Investigation of Mechanisms of High Lift for a Flat-Plate Airfoil undergoing Small-Amplitude Plunging Oscillations

D.J. Cleaver[1], Z. Wang[1], and I. Gursul[2]
University of Bath, Bath, United Kingdom, BA2 7AY

Two high lift mechanisms, convected leading-edge vortices (LEVs) and stable deflected jets, have previously been identified for an airfoil undergoing small-amplitude plunging oscillations. This paper extends this work by investigating the effect of geometry through direct comparison of the forces and flow fields associated with small-amplitude plunging oscillations of a NACA 0012 airfoil and flat plate for zero and a post-stall angle of attack of fifteen degrees, and a Reynolds number of 10,000. For zero degrees at high Strouhal numbers the NACA airfoil experiences stable deflected jets responsible for very large lift coefficients, whereas the flat plate experiences deflected jets that are prone to periodic oscillation in direction resulting in oscillation of the lift coefficient with a period on the order of 100 cycles. It is postulated that this jet switching is driven by the LEV. At fifteen degrees angle of attack the flat plate is shown to produce a comparable increase in lift up to a Strouhal number of unity but after this the lift performance deteriorates. This is due to the LEVs convecting further from the upper surface. At higher plunge velocities a new mode of LEV behavior is observed. The upper surface LEV pairs with the lower surface LEV to form a dipole that convects against the free stream and is rapidly dissipated. This results in a highly separated time-averaged flow and thus low lift and high drag.

[1] Lecturer, Department of Mechanical Engineering, Member AIAA.
[2] Professor, Department of Mechanical Engineering, Associate Fellow AIAA.

Nomenclature

a = amplitude of plunging motion

A = peak to peak amplitude of plunging motion

$\bar{C}_d$ = time-averaged drag coefficient

$\bar{C}_l$ = time-averaged lift coefficient

$\langle C_l \rangle$ = period-averaged lift coefficient

c = chord length

f = frequency

h = airfoil position

Re = Reynolds number, $\rho U_\infty c / \mu$

Sr_c = Strouhal number based on chord, fc/U_∞

Sr_A = Strouhal number based on amplitude, $2fa/U_\infty$

t = time, $t = 0$ is top of motion

T = plunge period

U_∞ = free stream velocity

V = velocity magnitude

x_{TEV} = streamwise position of trailing-edge vortex

y_{TEV} = cross-stream position of trailing-edge vortex

α = angle of attack

Γ = circulation

μ = viscosity

ρ = density

I. Introduction

There is currently growing interest in the field of Micro Air Vehicles (MAVs) due to their potential for a wide variety of applications both military and civil. However, for MAVs to become a practical reality it will first be necessary to move beyond the assumption of steady-state aerodynamics so as to overcome the prevalence of separation and stall at the low Reynolds numbers typical of micro air vehicles. Natural flyers have managed to circumvent this barrier through the exploitation of unsteady aerodynamic phenomenon [1], in particular the Leading Edge Vortex (LEV). The benefit of this approach can be seen in the truly exceptional agility of natural flyers over a wide range of Reynolds numbers. However, the large-amplitude, low-frequency motion suited to the muscular actuators of nature is not necessarily appropriate for the electrical actuators available to man. Instead small-amplitude high-frequency motion can be used to achieve similar plunge velocities in a more suitable manner.

Previous results for a NACA 0012 airfoil oscillating with small amplitude ($a/c \leq 0.2$) have identified two high lift mechanisms [2,3]. For a post-stall angle of attack, $\alpha = 15°$, high lift was due to LEVs that convect close to the airfoil's upper surface. This was termed a mode-1 flow field (see Fig. 1a). In addition significant drag reduction was observed resulting in thrust at higher Strouhal numbers. The switch from drag to thrust was shown to depend on the formation of what was termed a mode-2 flow field. This is a flow field where an upper surface clockwise LEV forms during the downward motion but instead of convecting over the upper surface, it remains near the leading-edge and loses its coherency through impingement with the upward moving airfoil.

The second high lift mechanism is associated with stable deflected jets and applies to smaller angles of attack: $\alpha \leq 10°$ (see Fig. 1b). The direction of the jet depends on the initial conditions

and creates significant bifurcations in the time-averaged lift coefficient. With a downward deflected jet large negative lift coefficients were observed; with an upward deflected jet very large positive lift coefficients of up to C_l = 5.5 were observed [3]. Deflected jets are a result of pairing of the trailing-edge vortices to create a vortex dipole. Due to asymmetric positioning, the dipole convects at an angle to the horizontal creating a deflected jet [3-9].

In this paper we will consider the effect of airfoil geometry on lift enhancement mechanisms for small-amplitude high-frequency motion. As thin airfoils are generally preferable at low Reynolds numbers [10], we shall compare the previous results for the NACA 0012 airfoil with new results for a flat plate geometry. We shall focus on two angles of attack, α = 0° to study the effect on deflected jets, and α = 15° to study the effect on post-stall performance.

II. Experimental Apparatus and Procedures

Force and Particle Image Velocimetry (PIV) measurements were conducted on a plunging flat plate airfoil mounted vertically in a closed-loop water tunnel, see Fig. 2. For a review of parameters studied, see Table 1; uncertainties are calculated using the methods of Moffat [11] taking into account both bias and precision errors.

Table 1 Experimental Parameters

Parameter	Range Considered	Uncertainty
Re	10,000	+/- 200
α	0° and 15°	+/- 0.5°
a/c	0.025 to 0.200	+/- 0.003
Sr_c	0 to 3	+/- 2.3%

Strouhal number is also directly related to the reduced frequency through: $Sr_c = k/\pi$.

A. Experimental Setup

The experiments were conducted in a free-surface closed-loop water tunnel (Eidetics Model 1520) at the University of Bath. The water tunnel is capable of flow speeds in the range 0 to 0.5 m/s and has a working section of dimensions 381 mm x 508 mm x 1530 mm. The turbulence intensity has previously been measured [12] by LDV to be less than 0.5%.

In this study two cross sections were considered: a NACA 0012 airfoil and a flat plate of thickness 0.04c with semi-circular leading and trailing edges, see Fig. 3. The flat plate was machined from 4 mm mild steel sheet and the NACA 0012 wing was selective laser sintered from Duraform Prototype PA with mild steel bars to guarantee spanwise rigidity. The wings have dimensions of 0.1 m chord x 0.3 m span, and were mounted vertically in a 'shaker' mechanism, see Fig. 2. They were placed between an upper and lower splitter plate, with clearances maintained at 2 mm. The oscillations were supplied via a Motavario 0.37 kW three-phase motor, 5:1 wormgear and IMO Jaguar Controller. The position of the root of the airfoil was measured through a rotary encoder attached to the spindle of the worm gear shaft. The rotary encoder was also used to trigger the PIV system.

B. Force Measurements

The forces applied in both the streamwise and cross-stream directions were measured via a two-component binocular strain gauge force balance [13]. The measured forces included both time-dependent aerodynamic forces as well as inertia forces, however the inertia forces do not contribute to the time-averaged force. Up to four force balances of differing rigidities were used so as to achieve the desired accuracy whilst minimizing flexibility. The signal from the strain gauges was amplified by a Wheatstone bridge circuit and sampled at either 2 kHz for 20,000

samples (stationary cases), or 360 per cycle for a minimum of 50 cycles (dynamic cases). The forces were then calculated from the average voltage through linear calibration curves. To minimize uncertainty the calibration curves consisted of twenty three points, and were performed daily before and after testing. Each data set was repeated at least once and then averaged. The mean lift coefficient uncertainty for the stationary case is ± 0.03.

C. PIV Measurements

The flow was seeded with 8 – 12 μm hollow glass spheres. The velocity field around the airfoil was measured using a TSI Inc. 2D-PIV system incorporating a dual ND:YAG 50 mJ pulsed laser, 2 MP Powerview Plus 12 bit CCD camera and TSI Model 610034 synchronizer. For measurements over the upper surface of the airfoil, the laser was positioned behind as shown in Fig. 2a. The shadow created by the airfoil therefore obscured the lower surface. For measurements over the lower surface the laser was positioned near the side wall of the tunnel as shown in Fig. 2b. In both cases, the camera was located under the tunnel. The PIV images were analyzed using the software Insight 3G. An FFT correlator was selected to generate a vector field of 199 x 148 vectors giving approximately a 1.2 mm spatial resolution for the upper surface, and 0.9 mm for the lower surface. The time-averaged data is derived from 500 pairs of images, the phase-averaged from 100 pairs for the upper surface and up to 250 pairs (as required) for the lower surface. The upper and lower surface data were later merged through interpolation of the upper surface data onto the lower surface grid in MATLAB.

III. Results and Discussion

A. Stationary Airfoil

The lift coefficient for the stationary two-dimensional NACA 0012 airfoil and flat plate are presented in Fig. 4. The shape of the NACA 0012 lift curve has previously been discussed and compared to results in the literature [14]. The nonlinear shape is indicative of trailing-edge stall which commences in the region of $\alpha = 1°$, becoming fully stalled once $\alpha > 10°$. This description was supported by PIV measurements and in agreement with the results of other authors [15,16]. By comparison the curve for the flat plate airfoil is very linear. Also shown are the experimental results of Sunada et al. [17] and Okamoto and Azuma [18] for a finite flat plate wing of aspect ratios: AR = 7.25 and 8 respectively, and Reynolds numbers: Re = 4,000 and 11,600. In addition, the linear trend predicted by the thin airfoil theory is shown as a solid line. The current data matches this trend to within the bounds of experimental uncertainty. The two finite wing cases break from this linear trend earlier resulting in a more gradual stall behavior. Despite this difference all three sets of experimental data reveal the stall in the vicinity of $\alpha \approx 9°$. For the angles of attack under consideration in this paper, $\alpha = 15°$ can therefore be classified as post-stall with the flat plate airfoil producing significantly more lift than the NACA 0012 airfoil and $\alpha = 0°$ predictably results in $C_l \approx 0$ due to the symmetry of the cross sections.

B. Deflected Jets ($\alpha = 0°$)

Shown in Fig. 5 is the time-averaged lift coefficient for a NACA 0012 airfoil oscillating at a range of Strouhal number, amplitude of a/c = 0.150, and $\alpha = 0°$. Solid lines represent data collected by starting at $Sr_c = 0$ (stationary), and increasing the Strouhal number very slowly, recording data at discrete points along the way. At each data point, we wait for sufficient settling

time and then measure the time-averaged forces. Then we move to a new frequency and repeat the procedure. Dashed lines represent data collected by impulsively starting at the maximum Strouhal number, and then decreasing the Strouhal number very slowly, recording data at discrete points along the way. In Figure 5 there are three types of curves: one for increasing frequency; and two for decreasing frequency where two starting positions: $h_i = +a$ and $h_i = -a$ are considered. Different runs correspond to the experiments performed at different times. Up to $Sr_c = 1.5$ all the curves match closely. After $Sr_c = 1.5$ the curves bifurcate producing two distinct results: increasing and decreasing ($h_i = a$) frequency produce very large positive lift coefficients; decreasing ($h_i = -a$) frequency produces very large negative lift coefficients. Hence for the same experimental conditions two entirely different results are possible; indeed the two results are approximate mirror images of each other in the x-axis. These are termed dual flows, with the positive lift coefficient branch termed mode-A and the negative branch termed mode-B [3]. Figure 5 also shows that the branches are highly repeatable.

Figure 6, which is adapted from Reference [3], shows PIV measurements for the NACA 0012 airfoil oscillating with $a/c = 0.15$ and $\alpha = 0°$ demonstrating a pre-bifurcation flow field (left column), mode-A flow field (central column), and mode-B flow field (right column). The time-averaged velocity magnitude (top row) for the pre-bifurcation flowfield shows a time-averaged jet aligned horizontally. The associated phase-averaged vorticity flowfields demonstrate this jet to be the result of a reverse-Kármán vortex street. During the downward motion (a to c) a counter-clockwise vortex forms and sheds from the trailing-edge; during the upward motion (c to a) a clockwise vortex forms. Both of these vortices convect along a path approximately aligned with the horizontal with equidistant spacing. At the leading-edge an upper surface clockwise vortex forms during the downward motion (see c) and loses its coherency during the upward

motion through impingement with the upward moving airfoil as previously described by Visbal [19] and Cleaver et al. [2]. Conversely during the upward motion a counter-clockwise leading-edge vortex forms (see a) and is dissipated during the downward motion. The flowfield as a whole is characterized by symmetry about the horizontal plane confirming the near-zero time-averaged lift coefficient.

With the Strouhal number increased into the dual-flow regime this symmetry is broken. In the mode-A case (central column) the time-averaged jet is deflected upwards and there is a time-averaged high velocity region over the upper surface. In the mode-B case (right column) the inverse is true, a downward deflected jet and a high velocity leading-edge region over the lower surface. The phase-averaged vorticity plots identify the cause to be trailing-edge vortex dipole formation. In the mode-A case (centre column) the clockwise TEV forms during the upward motion (c to a) and loiters near the airfoil during the downward motion (a to c) during which the counter-clockwise TEV forms. As a result of their proximity the vortices form a dipole that due to the relative positions of the vortices has a self-induced velocity in the upward direction, thereby creating an upward deflected jet. In the mode-B case (right column) the inverse is true, i.e., the counter-clockwise TEV 'loiters' creating a vortex dipole with a downward self-induced velocity and therefore a downward deflected jet. The mode-B flowfield therefore appears mirrored in the horizontal and out-of-phase with the mode-A case (compare Fig. 6c (centre) with Fig. 6a (right)).

Asymmetry of the flow near the trailing-edge influences the induced velocity near the leading-edge. In the mode-A case there is a strong upper surface LEV (Fig. 6c centre), and a comparatively weak lower surface LEV (Fig. 6a centre, supported by circulation measurements not shown here). This explains both the high velocity leading-edge region observed in the time-

averaged plot and very high lift coefficient observed for this case, $C_l \approx 3.4$. For the mode-B case the inverse is true, i.e., a weak upper surface LEV and strong lower surface LEV resulting in a large negative lift coefficient.

Now moving onto the flat plate airfoil, Figure 7 shows the same measurements as in Fig. 5 except for the flat plate airfoil. Up until $Sr_c = 1.5$ all curves match closely, following similar trends to those observed for the NACA 0012 airfoil. After $Sr_c = 1.5$, however, the different tests performed at different times diverge giving very erratic results with no repeatability. Despite the apparent randomness, these results fall within an upper and lower bound which bears a strong resemblance to that for the NACA 0012 airfoil, and with the same point of divergence. This suggests that deflected jets are also responsible in this case but that their direction is unstable, in a similar manner to the jet switching phenomenon of Heathcote and Gursul [6].

Force measurements were therefore performed over a much larger time period for the flat plate; but with the signal averaged over individual periods instead of over the whole time period, see Fig. 8. This figure demonstrates that the period-averaged lift force oscillates approximately sinusoidally with amplitude of $C_l \approx 5$ and period on the order of 100 plunge cycles. Using a sample size of 60 cycles as in Fig. 7 is therefore insufficient to accurately capture an average. This explains the scatter in the time-averaged data in Fig. 7 when the jet is oscillating in direction. The period of this oscillation correlates well with the values observed by Heathcote and Gursul [6] for periodic jet switching of rigid and flexible airfoils oscillating in still fluid.

To capture the phenomenon responsible for the oscillatory lift coefficient, phase-locked instantaneous PIV measurements were performed in conjunction with simultaneous force measurements, a selection are shown in Fig. 9. These PIV measurements were all taken when $h = -a$. The flow field in the top row shows a vortex dipole pairing that due to its position would

result in a downwards deflected jet. The period-averaged lift coefficient in this case is C_l = -5.1. The correlation between downward deflected jet and large negative lift coefficient mirrors that observed for the NACA 0012 airfoil. In the next row the TEV behavior is significantly different. The vortices are not paired and instead convect approximately horizontally. The lift coefficient for this case is C_l = -1.1. In the next time there is now an established upwards deflected jet with close vortex pairings which coincides with a lift coefficient of C_l = 5.5. Figure 9 therefore clearly demonstrates that the flat plate is subject to jet switching with the downward deflected jet associated with very large negative lift coefficients and upwards deflected jets very large positive lift coefficients. Animations of the process show the transition from one to the other to be gradual, not distinct, confirming the approximately sinusoidal variation in lift coefficient observed in Fig. 8.

As further evidence of the existence of jet switching the position and circulation of the trailing-edge vortices in the instantaneous phase-locked PIV results were measured, see Fig. 10. Figure 10a shows the vertical position of both the clockwise and counter-clockwise TEV, see Fig. 10c for an example flow field. The position of both clockwise and counter-clockwise TEV clearly oscillates almost sinusoidally with a period on the order of 100T. Indeed a sine curve fitted to the clockwise vortex y_{TEV} position gives a period of 102T. Likewise the normalized circulation of the TEVs also oscillates with a period of approximately 100T although the trend is not as pronounced, see Fig. 10b. Using these instantaneous measurements it is possible to make a direct comparison between the NACA 0012 bifurcation modes and their flat plate equivalents. The equivalents are defined by the position, y_{TEV}, of the clockwise vortex (see Fig. 10a). From 500 instantaneous flow fields, the 50 flow fields (10% of total) with the largest clockwise y_{TEV} values are defined as mode A equivalent (upward deflected jet), and the 50 instantaneous

flowfields (10%) with the smallest clockwise y_{TEV} values are defined as mode B equivalent (downward deflected jet). Using this definition a comparison of phase-averaged NACA flowfields and their flat plate equivalents is shown in Fig. 11.

Figure 11 demonstrates that despite the differences in geometry the trailing-edge vortices are qualitatively similar. For mode A, for both geometries the vortex pairing is indicative of an upwards deflected jet, and for mode B, the vortex pairing is indicative of a downwards deflected jet. The position and strength of the trailing-edge vortices is similar between the two flowfields, this is quantified in Table 2. However, it is obvious in Figure 11 that the location of the leading-edge vortex differs substantially.

Table 2 Comparison of the mean instantaneous trailing-edge vortex characteristics for the NACA 0012 bifurcation flowfields and their flat plate equivalents for the single phase h = -a.

		Clockwise TEV			Counter-Clockwise TEV		
		x_{TEV}/c	y_{TEV}/c	$\Gamma/U_\infty c$	x_{TEV}/c	y_{TEV}/c	$\Gamma/U_\infty c$
A	NACA 0012	**0.68**	**0.15**	**-4.12**	**0.44**	**0.48**	**3.62**
	Flat Plate	**0.67**	**0.14**	**-3.71**	**0.40**	**0.41**	**3.90**
B	NACA 0012	**1.04**	**-0.35**	**-2.98**	**0.16**	**0.31**	**4.33**
	Flat Plate	**0.94**	**-0.37**	**-2.81**	**0.16**	**0.26**	**4.55**

The core question is therefore what aspect of the flat plate geometry makes it subject to jet switching when the NACA 0012 airfoil at the same conditions is not. As deflected jets and TEV dipole formation are a prerequisite for jet switching, the intuitive choice is the difference in trailing-edge geometry (sharp versus rounded). To investigate this possibility a further flat plate wing was manufactured with a sharp trailing edge. Until x/c = 0.7 the geometry was identical to the flat plate airfoil, after x/c = 0.7 it tapers linearly to a sharp point. Force measurements showed this wing to also be subject to jet switching, with a similar period. Hence, as trailing-edge geometry has no effect on the jet-switching phenomenon, and the TEVs are similar but the LEVs

are different in Fig. 11, we postulate that jet switching is due to the different behavior of the LEVs and that this is merely reflected in the TEV behavior. Further observations on the different behavior of the LEVs are also documented in the next section.

Similar lift measurements were also performed for three further amplitudes, a/c = 0.025, 0.100 and 0.200 (not shown here). Jet switching behavior was observed for a/c = 0.100 and 0.200 with the same point of bifurcation as the NACA 0012 airfoil. Hence, these unstable deflected jets are a major disadvantage for the flat-plate airfoils in MAV applications. For a/c = 0.025 bifurcation was not observed presumably for the same reason bifurcation was not observed for the NACA 0012 airfoil at this amplitude, i.e., the maximum Strouhal number tested was insufficient [3].

C. Convected Leading Edge Vortices (α = 15°)

Shown in Fig. 12 is the time-averaged lift, and drag coefficient for a NACA 0012 airfoil (left column) and flat plate (right column) oscillated at a post-stall angle of attack of α = 15°, range of amplitudes and range of Strouhal numbers. Starting with the NACA 0012 airfoil, both lift and drag coefficients are discussed elsewhere [2]. At low Strouhal numbers, small-amplitude airfoil oscillations increase lift coefficient significantly with greater effect for greater amplitude. The largest increase observed is therefore for the largest amplitude of a/c = 0.2 and 305% over the value for a stationary airfoil. It was shown that this lift increase is approximately proportional to the non-dimensional plunge velocity, $Sr_A = fA/U_\infty$, and that superimposed onto this linear trend are local optima. These can be seen as the peaks at $Sr_c \approx 0.5$, 1, and 2. Hot-film measurements showed these to be due to resonance with the natural shedding frequency, its harmonics and subharmonics. At higher Strouhal numbers this linear trend is broken by a significant fall in lift,

this can be seen around $Sr_c \approx 1.15$ for $a/c = 0.2$, $Sr_c \approx 1.5$ for $a/c = 0.15$, and $Sr_c \approx 2.0$ for $a/c = 0.1$. The cause of this fall has been shown to be a combination of the dissipation of the upper surface LEV and formation of a lower surface LEV. Small-amplitude airfoil oscillations can also improve drag performance significantly with greater effect for greater amplitude, see Fig. 12b left. The improvement is such that for the four larger amplitudes thrust is observed at higher Strouhal numbers. The switch from drag to thrust was shown to be highly dependent on the formation of what was termed a mode-2 flow field. This is characterized by the formation of an upper surface leading-edge vortex during the airfoil's downward motion and then its dissipation during the upward motion, as opposed to its convection into the wake in a mode-1 flow field.

Now considering the force measurements for the flat plate, the results are shown in Fig. 12 right column. Lift coefficient demonstrates the first two peaks at the same Strouhal numbers as for the NACA 0012 airfoil, $Sr_c \approx 0.5$ and 1. This would be expected as when the flow is fully separated the natural shedding frequency is determined by the frontal area [20,21] and for $\alpha = 15°$ this is almost identical for the NACA 0012 airfoil and flat plate. A second interesting feature is in contrast to the sudden fall in lift observed for the NACA 0012 airfoil, there is a gradual deterioration in lift with onset around $Sr_c = 1$. Drag coefficient demonstrates significantly worse performance for the flat plate. Indeed in comparison with the NACA 0012 airfoil there is essentially no reduction in drag coefficient, and as a result there is no switch from drag to thrust for any amplitude.

Shown in Fig. 13 is the time-averaged velocity magnitude for both the NACA 0012 airfoil (left column) and flat plate (right column) for $\alpha = 15°$, $a/c = 0.025$ and range of Strouhal numbers. Figure 13a (left) presents the streamlines and the magnitude of the total velocity vector for the stationary NACA0012 airfoil at an angle of attack of $\alpha = 15°$. There is a large region of

separation over the suction surface of the airfoil. The airfoil can therefore be classified as fully stalled in agreement with the force measurements already presented, and other authors [16, 22]. The flat plate airfoil experiences a similar region of separation, although due to the smaller radius of curvature at the leading-edge, the point of separation is closer to the leading-edge. Oscillation even at small amplitude (a/c = 0.025) and low frequency (Sr_c = 0.25 and 0.50) significantly reduces this separated region, see Fig. 13b and c. It is worth noting that due to the nature of time-averaged measurements the motion of the airfoil obscures the region in its direct vicinity. This makes the separated region appear smaller than is necessarily true. It is therefore preferable to consider the mean position (shown with solid line) when comparing against the stationary case. Even taking this into account the separation reduction is still significant for both NACA 0012 airfoil and flat plate. The reduction is however greater for the flat plate airfoil as is reflected in the measured lift coefficient, ΔC_l = 0.5 versus ΔC_l = 0.38 for Sr_c = 0.50. For both geometries there is also a high velocity leading-edge region suggesting LEV formation.

With the Strouhal number increased to Sr_c = 1 (Fig. 13e) the high velocity leading-edge region is enhanced for both NACA 0012 airfoil and flat plate airfoil. For the NACA 0012 airfoil the reduction in separation has continued however for the flat plate, even though the nature of the separation has changed there is no further noticeable reduction. For Strouhal numbers larger than Sr_c = 1 the flat plate experiences generally deteriorating lift performance whilst the NACA 0012 airfoil experiences generally improving lift performance. This trend is reflected for Sr_c = 1.25 to 3.0 in Fig. 13f to m. In contrast to the reducing separation of the NACA 0012 airfoil, the flat plate experiences increasing separation with increasing Strouhal number. In addition the high velocity leading-edge region becomes smaller for the flat plate and further from the upper surface. This trend of increased separation and decreased high velocity leading-edge region for

the flat plate continues up to $Sr_c = 3$. At $Sr_c = 3$ (Fig. 13m) for the first time for the NACA 0012 airfoil there is a time-averaged jet. This is indicative of thrust creation due to the action of a reverse-Kármán vortex street which is reflected in the drag coefficient measurements shown in Fig. 12b. By contrast the flat plate does not demonstrate a reverse-Kármán vortex street and therefore experiences a net drag.

To explain why there is such a difference between the geometries for $Sr_c > 1$, phase-averaged vorticity contour plots are shown in Fig. 14 at the top of the motion for the same amplitude as Fig. 13. Starting with $Sr_c = 1$ (Fig. 14a) for this case the increase in lift coefficient and reduction in separation is comparable for the NACA 0012 airfoil and flat plate airfoil, the phase-averaged flow fields, however, show significant differences. For the NACA 0012 airfoil there are two small clockwise LEVs close to the upper surface; whereas for the flat plate there is a single, larger, more diffuse clockwise LEV slightly further from the upper surface. In both cases these upper surface LEVs are formed during the downward motion before being shed and convected over the upper surface. The decreasing effective angle of attack in the second half of the upward motion combined with the action of the passing clockwise LEV initiates the formation of the counter-clockwise TEV seen at the trailing-edge in Fig. 14a.

With the Strouhal number increased to $Sr_c = 1.5$ the lift performance and separation reduction of the two has diverged. The phase-averaged flow fields (Fig. 14b) show the NACA 0012 airfoil to form a single clockwise LEV per cycle. This LEV is small, concentrated, and convects close to the surface. Conversely the flat plate also has a single clockwise LEV but it is larger, more diffuse, and convects further from the upper surface. Likewise the number of TEVs is similar for both geometries but they are generally larger, and more diffuse in the case of the flat plate.

With further increase in Strouhal number to Sr_c = 2.0 (Fig. 14c) these characteristics continue. There is a single LEV formed during each cycle but in the case of the flat plate airfoil the vortex is larger, more diffuse, convects more slowly (as suggested by the vortex spacing), and convects further from the upper surface. Due to the large vertical distance between the convecting LEV and trailing-edge it does not interact with the TEVs. It is also interesting to note that the LEV for the flat plate has a strong secondary vortex. Due to this secondary vortex the vortex pair remains nearer to the leading-edge for a greater proportion of the cycle.

With further increase in Strouhal number to Sr_c = 2.5 (Fig. 14d) and Sr_c = 3.0 (Fig. 14e), the difference is further enhanced. For the NACA 0012 airfoil the LEVs are small, concentrated and convect very close to the upper surface interacting at the trailing-edge with the TEVs. Conversely for the flat plate the LEVs are larger, more diffuse, with a much stronger secondary vortex, and convect further from the upper surface. The reason for the deteriorating lift performance of the flat plate at high Strouhal numbers can therefore be attributed to the trajectory of the LEV. As it is further from the airfoil surface, its lift enhancing effect will be significantly weakened and there will be greater time-averaged separation. In essence the NACA 0012 geometry utilizes the LEV in a more effective way.

In Fig. 14 the maximum Strouhal number based on amplitude was Sr_A = 0.15 for the small amplitude motion (a/c = 0.025). Shown in Fig. 15 are similar phase-averaged measurements for a larger amplitude (a/c = 0.15), which allowed for larger plunge velocities, i.e., $Sr_A \leq 0.6$. New types of flow behavior are therefore observed. For $Sr_c \leq 1$ the principal differences are the same as for the smaller amplitude previously discussed. For both geometries an upper surface LEV forms during the downward motion, but for the flat plate it is more diffuse, and convects further from the upper surface. For $Sr_c > 1$ one begins to observe new behavior, instead of the vortex

dissipation typical of a mode-2 flowfield, the upper-surface LEV never appears to form for the flat plate airfoil, see Fig. 15c and Fig. 15d. The only visible clockwise vorticity is a vague region above the leading-edge that appears as a ‘plume’.

Figure 16 shows this process in more detail covering both the upper and lower surface for the same amplitude and Strouhal number combination as in Fig. 15d. The vorticity fields are in a counter-clockwise loop starting at the top of the motion in the top left corner, moving down through the left column to the bottom of the motion in the bottom right, and then up through the right column back to the start. At $t/T = 0$ there is a clear, strong counter-clockwise lower surface LEV. This interacts with the boundary-layer to form clockwise vorticity. During the initial stages of the downward motion ($t/T = 0$ to 2/12) this clockwise vorticity forms a vortex that pinches off by the point of maximum effective angle of attack ($t/T = 3/12$). This clockwise vortex pairs with the counter-clockwise to create a vortex dipole that convects away from the leading-edge in an upstream direction ($t/T = 2/12$ to 7/12). During this time both vortices rapidly dissipate. This dissipation in the phase-averaged flow is an indication of the vortices becoming highly three-dimensional.

This behavior is in stark contrast to the NACA 0012 airfoil, a direct comparison is shown in Fig. 17. The NACA 0012 airfoil shows a clockwise upper surface LEV forms during the downward motion, before losing its coherency during the upward motion. Likewise a counter-clockwise lower surface LEV forms during the upward motion and has already started to lose its coherency at the top of the motion. There is no sign of interaction between the upper and lower surface LEV.

The growth and dissipation of the LEVs is quantified in Fig. 18. The NACA 0012 airfoil is denoted by solid symbols and lines. The growth of the upper surface clockwise LEV for the

NACA airfoil is shown in the range t/T = 0 to 0.375 where it reaches its maximum strength of $\Gamma/U_\infty c$ = -2.90. After this the vortex decays rapidly through impingement with the upward moving airfoil. The lower surface counter-clockwise vortex likewise grows in the range t/T = 0.5 to 0.875 attaining its maximum value of $\Gamma/U_\infty c$ = 3.26, then decays rapidly through impingement with the downward moving airfoil. The growth phase for the flat plate clockwise vortex is similar to that for the NACA airfoil except the whole process is advanced by $t/T \approx 0.125$. This is due to the reinforcing effect of the counter-clockwise vortex visible at t/T = 0/12 to 2/12 in Fig. 18. The peak value is almost identical to the NACA airfoil, $\Gamma/U_\infty c$ = -2.88. The flat plate counter-clockwise vortex however is significantly different from its NACA counterpart. It is slightly advanced by $t/T \approx 0.05$, attaining a significantly higher peak circulation of $\Gamma/U_\infty c$ = 4.18, and then decays more slowly. The cause of dipole formation for the flat plate can therefore be attributed to the stronger lower surface vortex promoting premature formation of the upper surface vortex. This behavior is very similar to that previously described elsewhere [3], for TEV dipole formation on a NACA 0012 airfoil under similar conditions.

IV. Conclusions

Experiments were performed to compare the forces and flow fields of both a NACA 0012 airfoil and flat plate oscillating with small-amplitude at angles of attack of 0° and 15° to study two high-lift mechanisms: deflected jets and convected LEVs. For zero degrees angle of attack, at high Strouhal numbers, the NACA airfoil is subject to stable deflected jets resulting in very large negative or positive lift coefficients with the direction determined by initial conditions. The flat plate airfoil is likewise subject to deflected jets however the direction oscillates approximately sinusoidally between upwards and downwards with a period on the order of 100

cycles. The lift coefficient is therefore also oscillatory. This is considered to be a problem for the flat-plate airfoil in MAV applications. The results presented imply that it is the LEV rather than the TEV that drives the jet switching phenomenon.

For 15° angle of attack, at low Strouhal numbers, the force coefficients for the NACA airfoil and flat plate are similar. Both experience significant increase in lift coefficient with greater effect for greater amplitude and local optima due to resonance with the natural shedding frequency, its harmonics and subharmonics. This increase is associated with reduced time-averaged separation and a high velocity leading-edge region due to LEV formation and convection. However, after a Strouhal number of unity the flat plate experiences deteriorating lift performance across all amplitudes studied. At small amplitudes the deterioration in lift performance is primarily due to the LEV convecting further from the upper surface; at large amplitudes it is due to the LEVs forming a dipole which convects against the freestream resulting in increased time-averaged separation.

Acknowledgments

The work was sponsored by the Air Force Office of Scientific Research, Air Force Material Command, USAF under grant number FA8655-10-1-3093, as well as the Engineering and Physical Sciences Research Council (EPSRC) Studentship, and the RCUK Academic Fellowship in Unmanned Air Vehicles.

References

[1] Sane, S.P., "The Aerodynamics of Insect Flight," *Journal of Experimental Biology*, Vol. 206, No. 23, 2003, pp. 4191-4208.

[2] Cleaver, D.J., Wang, Z., Gursul, I., and Visbal, M.R., "Lift Enhancement by Means of Small Amplitude Airfoil Oscillations at Low Reynolds Numbers," *AIAA Journal*, Vol. 49, No. 9, 2011, pp. 2018 - 2033.

[3] Cleaver, D.J., Wang, Z., and Gursul, I., "Bifurcating Flows of Plunging Airfoils at High Strouhal Numbers," *Journal of Fluid Mechanics*, vol. 708, 2012, pp. 349-376.

[4] Jones, K.D., Dohring, C.M., and Platzer, M.F., "Experimental and Computational Investigation of the Knoller-Betz Effect," *AIAA Journal*, Vol. 36, No. 7, 1998, pp. 1240-1246.

[5] Lewin, G.C., and Haj-Hariri, H., "Modelling Thrust Generation of a Two-Dimensional Heaving Airfoil in a Viscous Flow," *Journal of Fluid Mechanics*, Vol. 492, 2003, pp. 339-362.

[6] Heathcote, S., and Gursul, I., "Jet Switching Phenomenon for a Periodically Plunging Airfoil," *Physics of Fluids*, Vol. 19, No. 2, 2007.

[7] Godoy-Diana, R., Aider, J.L., and Wesfreid, J.E., "Transitions in the Wake of a Flapping Foil," *Physical Review E*, Vol. 77, No. 1, 2008.

[8] von Ellenrieder, K.D., and Pothos, S., "PIV Measurements of the Asymmetric Wake of a Two Dimensional Heaving Hydrofoil," *Experiments in Fluids*, Vol. 44, No. 5, 2008, pp. 733-745.

[9] Godoy-Diana, R., Marais, C., Aider, J.L., and Wesfreid, J.E., "A Model for the Symmetry Breaking of the Reverse Benard-Von Karman Vortex Street Produced by a Flapping Foil," *Journal of Fluid Mechanics*, Vol. 622, 2009, pp. 23-32.

[10] Mueller, T. J., and DeLaurier, J. D., "An Overview of Micro Air Vehicles Aerodynamics," *Fixed and Flapping Wing Aerodynamics for Micro Air Vehicle Applications*, edited by T. J. Mueller, Vol. 195, Progress in Astronautics and Aeronautics, AIAA, Virginia, 2001, pp. 1-9.

[11] Moffat, R.J., "Using Uncertainty Analysis in the Planning of an Experiment," *Journal of Fluids Engineering - Transactions of the ASME*, Vol. 107, No. 2, 1985, pp. 173-178.

[12] Heathcote, S. "Flexible Flapping Airfoil Propulsion at Low Reynolds Numbers," *Ph.D. Dissertation*, Dept of Mechanical Engineering, University of Bath, Bath, 2006.

[13] Frampton, K.D., Goldfarb, M., Monopoli, D., and Cveticanin, D. "Passive Aeroelastic Tailoring for Optimal Flapping Wings," Proceedings of Conference on Fixed, Flapping and Rotary Wing Vehicles at Very Low Reynolds Numbers, 2000, pp. 473-482.

[14] Cleaver, D.J., Wang, Z., and Gursul, I. "Vortex Mode Bifurcation and Lift Force of a Plunging Airfoil at Low Reynolds Numbers," 48th AIAA Aerospace Sciences Meeting, AIAA 2010-390, 2010.

[15] Huang, R.F., and Lin, C.L., "Vortex Shedding and Shear-Layer Instability of Wing at Low-Reynolds Numbers," *AIAA Journal*, Vol. 33, No. 8, 1995, pp. 1398-1403.

[16] Sunada, S., Sakaguchi, A., and Kawachi, K., "Airfoil Section Characteristics at a Low Reynolds Number," *Journal of Fluids Engineering - Transactions of the ASME*, Vol. 119, No. 1, 1997, pp. 129-135.

[17] Sunada, S., Yasuda, T., Yasuda, K., and Kawachi, K., "Comparison of Wing Characteristics at an Ultralow Reynolds Number," *Journal of Aircraft*, Vol. 39, No. 2, 2002, pp. 331-338.

[18] Okamoto, M., and Azuma, A., "Aerodynamic Characteristics at Low Reynolds Numbers for Wings of Various Planforms," *AIAA Journal*, Vol. 49, No. 6, 2011, pp. 1135-1150.

[19] Visbal, M.R., "High-Fidelity Simulation of Transitional Flows Past a Plunging Airfoil," *AIAA Journal*, Vol. 47, No. 11, 2009, pp. 2685-2697.

[20] Fage, A., and Johansen, F.C., "On the Flow of Air Behind an Inclined Flat Plate of Infinite Span," *Proceedings of the Royal Society of London Series A*, Vol. 116, 1927, pp. 170-197.

[21] Abernathy, F.H., "Flow over an Inclined Plate," *Transactions of the ASME, Journal of Basic Engineering*, Vol. 84, 1962, pp. 380 - 388.

[22] Schluter, J.U. "Lift Enhancement at Low Reynolds Numbers Using Pop-up Feathers," 39th AIAA Fluid Dynamics Conference, AIAA Paper 2009-4195, 2009.

Figures

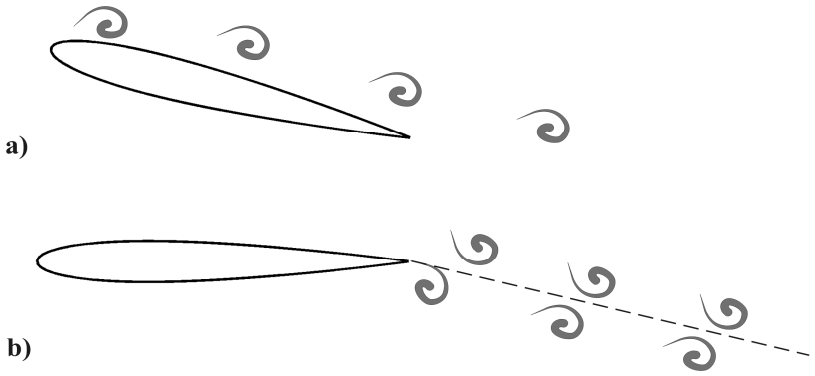

Fig. 1 High-lift mechanisms for a NACA 0012 airfoil oscillating with small-amplitude: a) convected LEV for post-stall angles of attack, and b) deflected jets for pre-stall angles of attack.

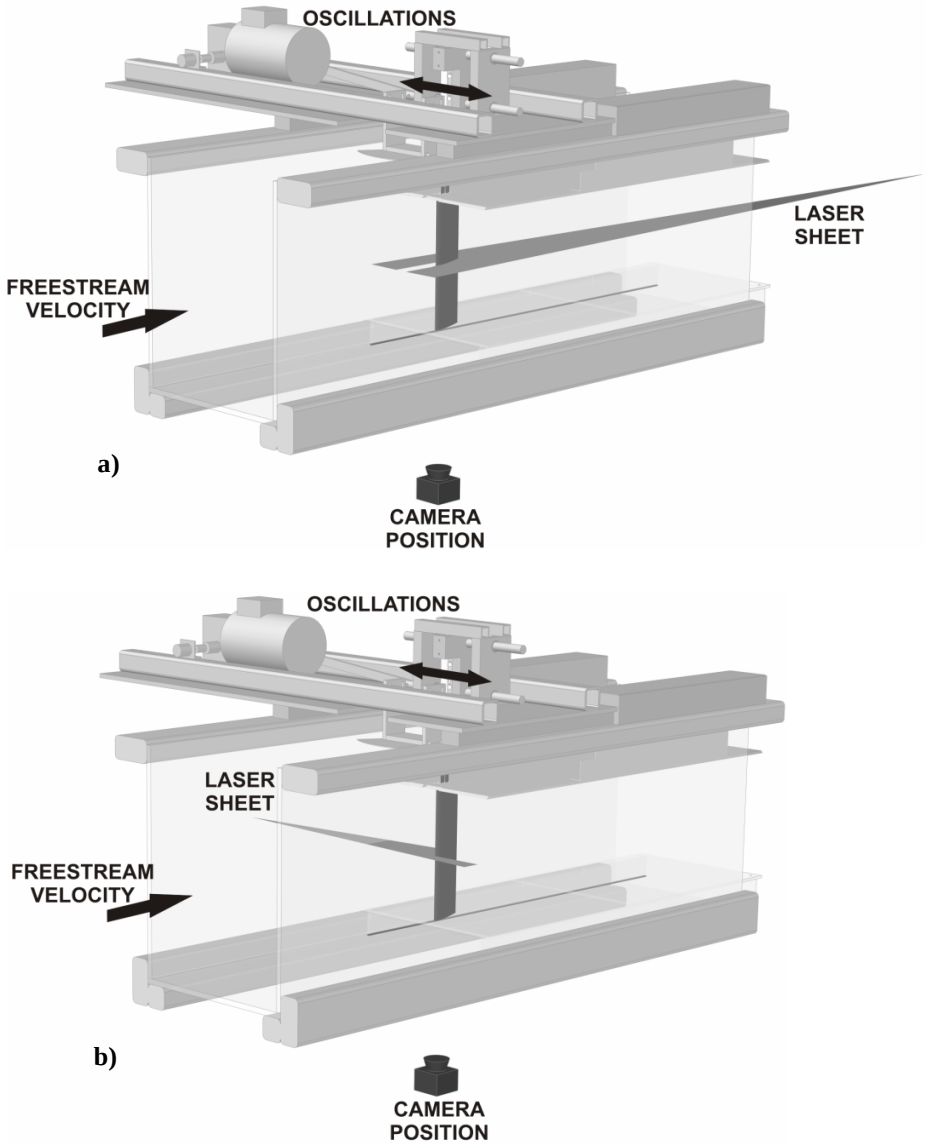

Fig. 2 Experimental setup a) for PIV measurements over the upper surface, and b) for PIV measurements over the lower surface.

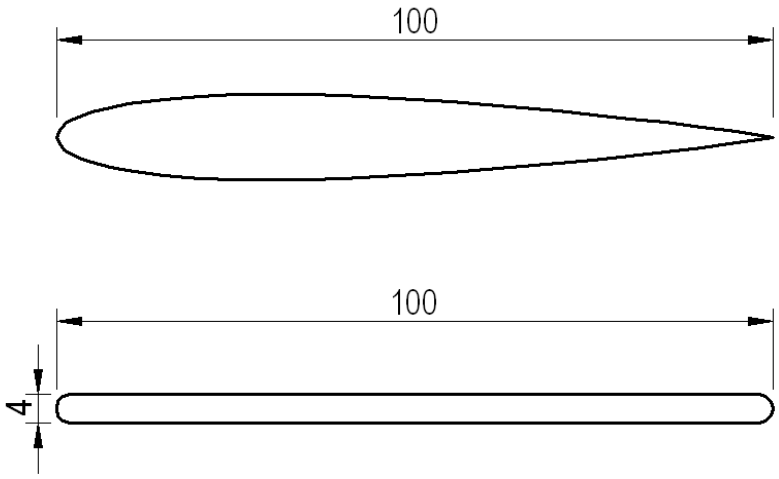

Fig. 3 Airfoil cross-section showing: NACA 0012 (top) and flat plate (bottom).

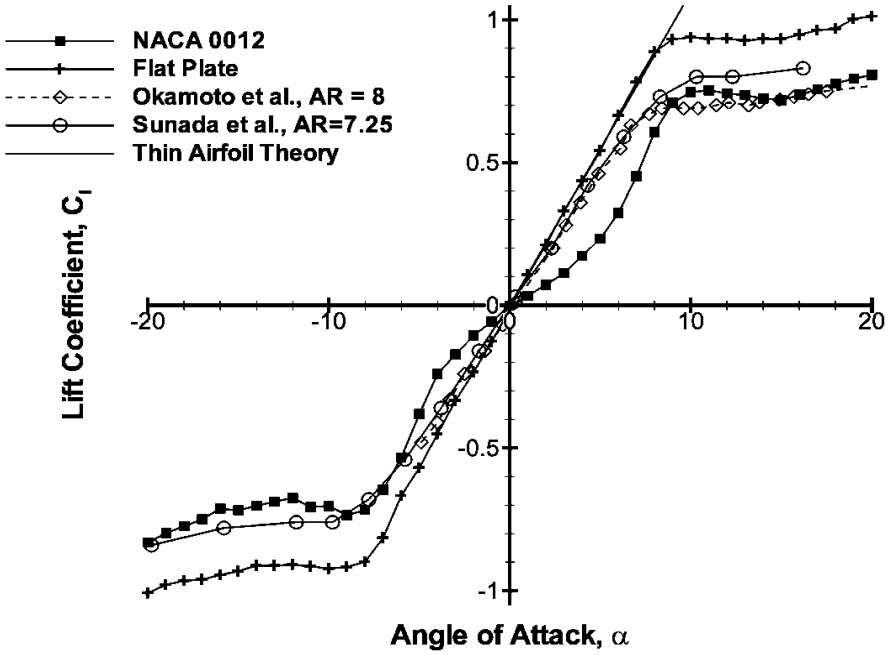

Fig. 4 Lift coefficient for the stationary NACA 0012 airfoil and flat plate airfoil at a Reynolds number of *Re* = 10,000. Also shown are curves for a flat plate airfoil from Okamato et al. (2011) for *Re* = 11,600, Sunada et al. (2002) for *Re* = 4,000 and thin airfoil theory.

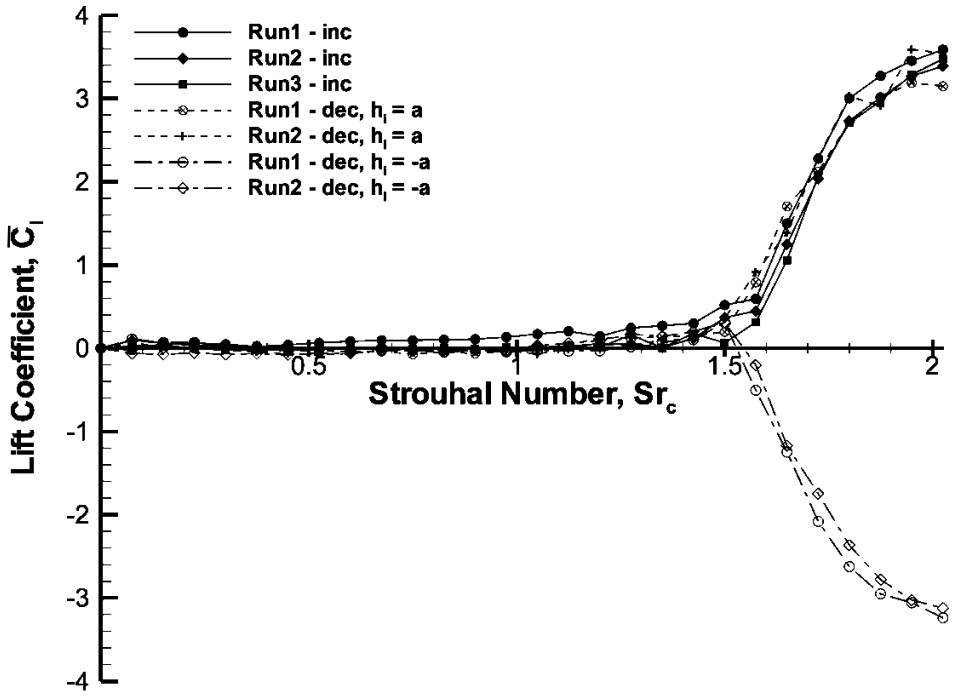

Fig. 5 Time-averaged lift coefficient for the NACA 0012 airfoil oscillating with *a/c* = 0.15 at α = 0°.

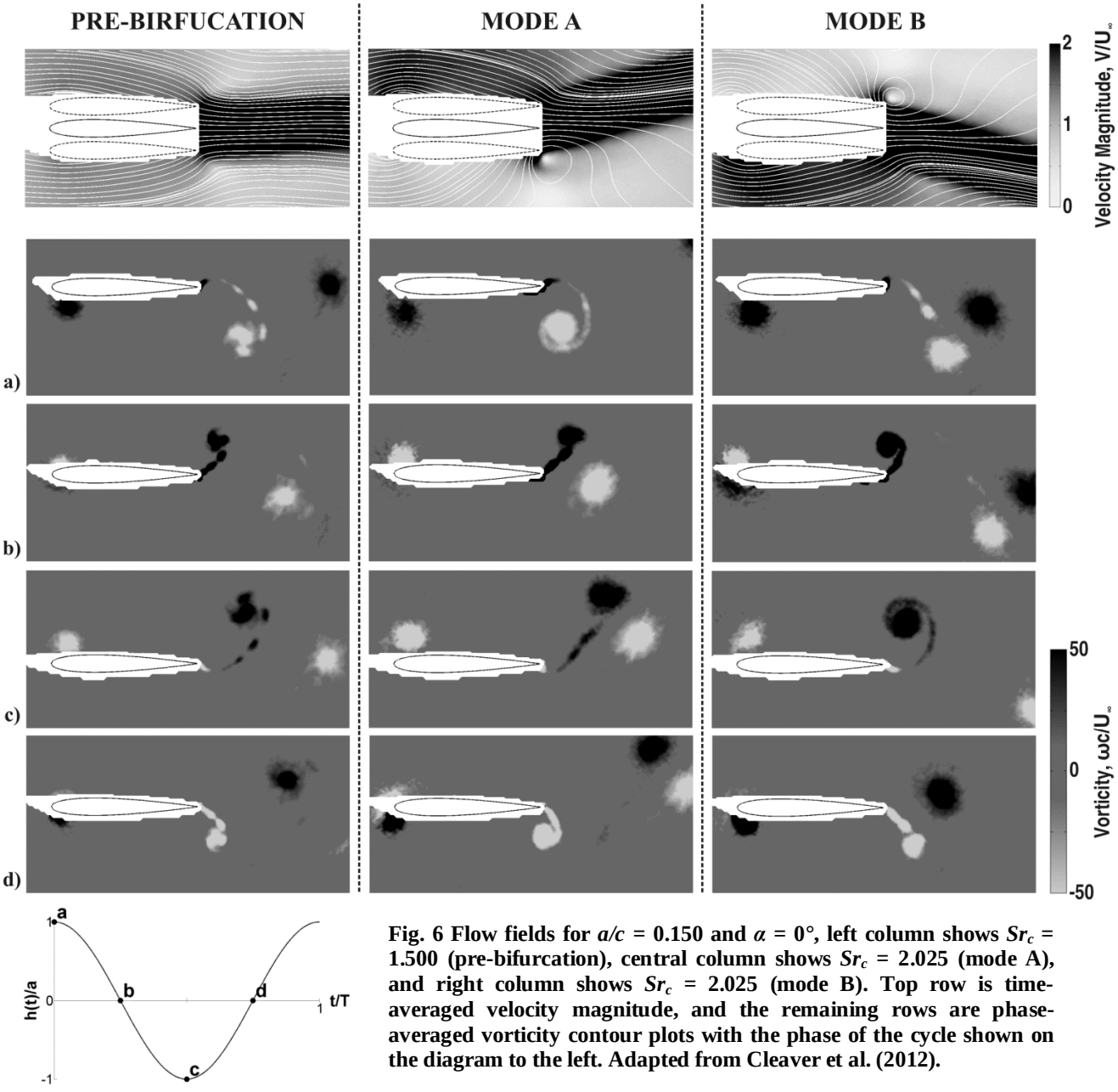

Fig. 6 Flow fields for a/c = 0.150 and α = 0°, left column shows Sr_c = 1.500 (pre-bifurcation), central column shows Sr_c = 2.025 (mode A), and right column shows Sr_c = 2.025 (mode B). Top row is time-averaged velocity magnitude, and the remaining rows are phase-averaged vorticity contour plots with the phase of the cycle shown on the diagram to the left. Adapted from Cleaver et al. (2012).

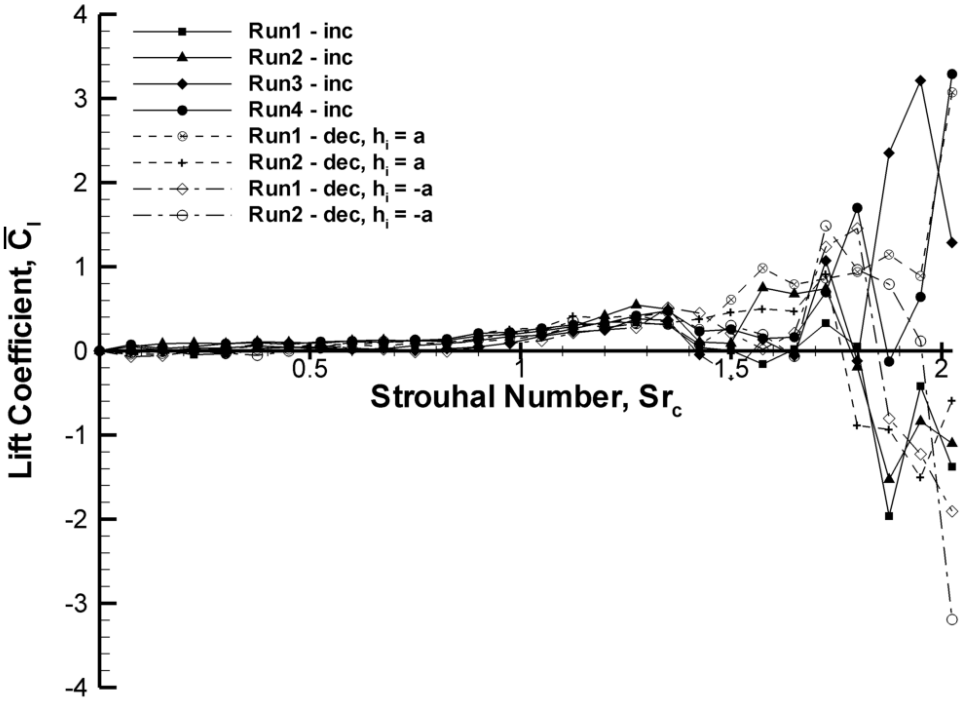

Fig. 7 Time-averaged lift coefficient for flat plate airfoil oscillating with *a/c* = 0.15 at α = 0°.

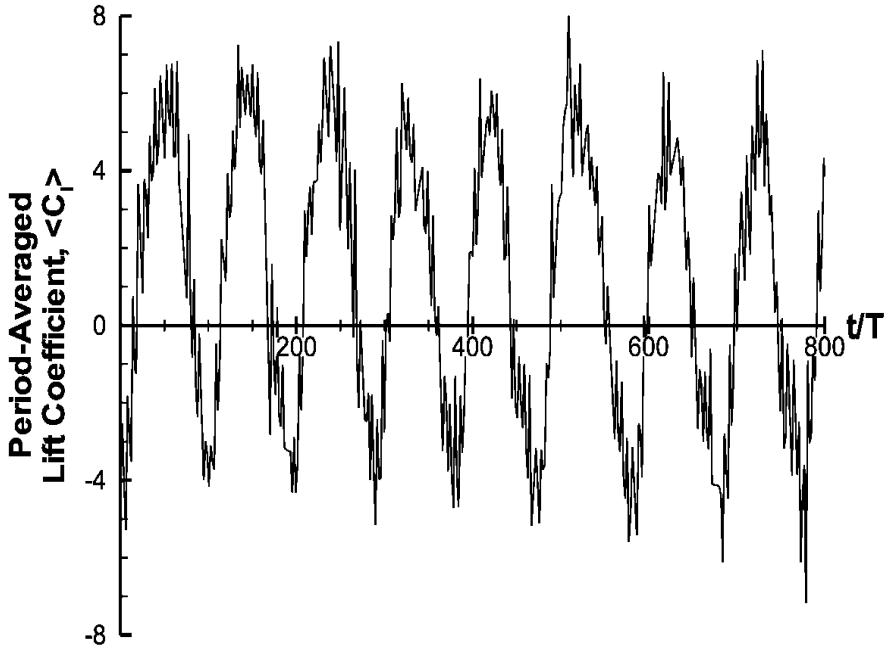

Fig. 8 Period-averaged lift coefficient for the flat plate oscillating at *a/c* = 0.15, Sr_c = 2.025, and α = 0°.

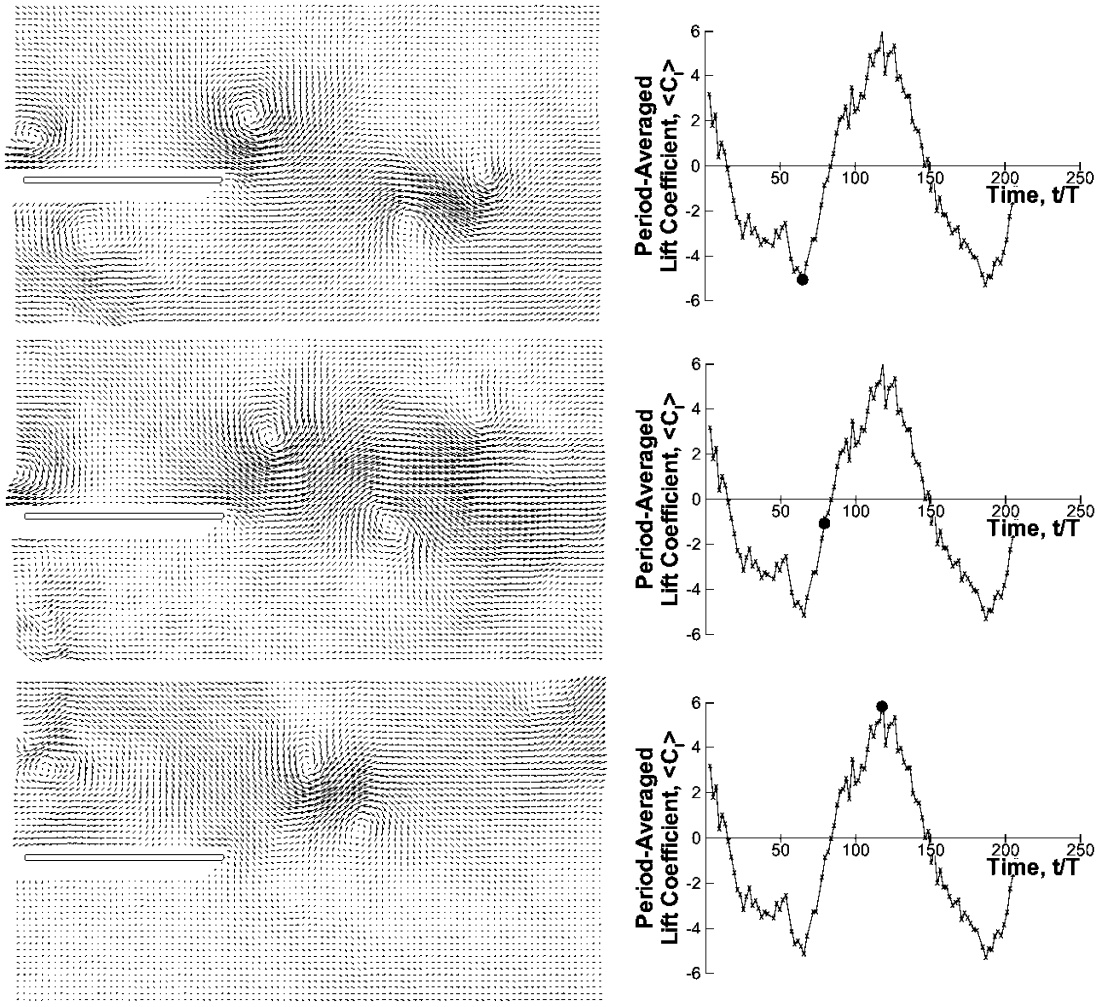

Fig. 9 Jet-switching phenomenon for the flat plate oscillating with $\alpha = 0°$, $Sr_c = 2.025$ and $a/c = 0.15$. Shown on the left are instantaneous flow field phase-locked to $h = -a$. Shown on the right are simultaneous period-averaged lift coefficient measurements with the time of the velocity vector plot denoted by a solid circular symbol.

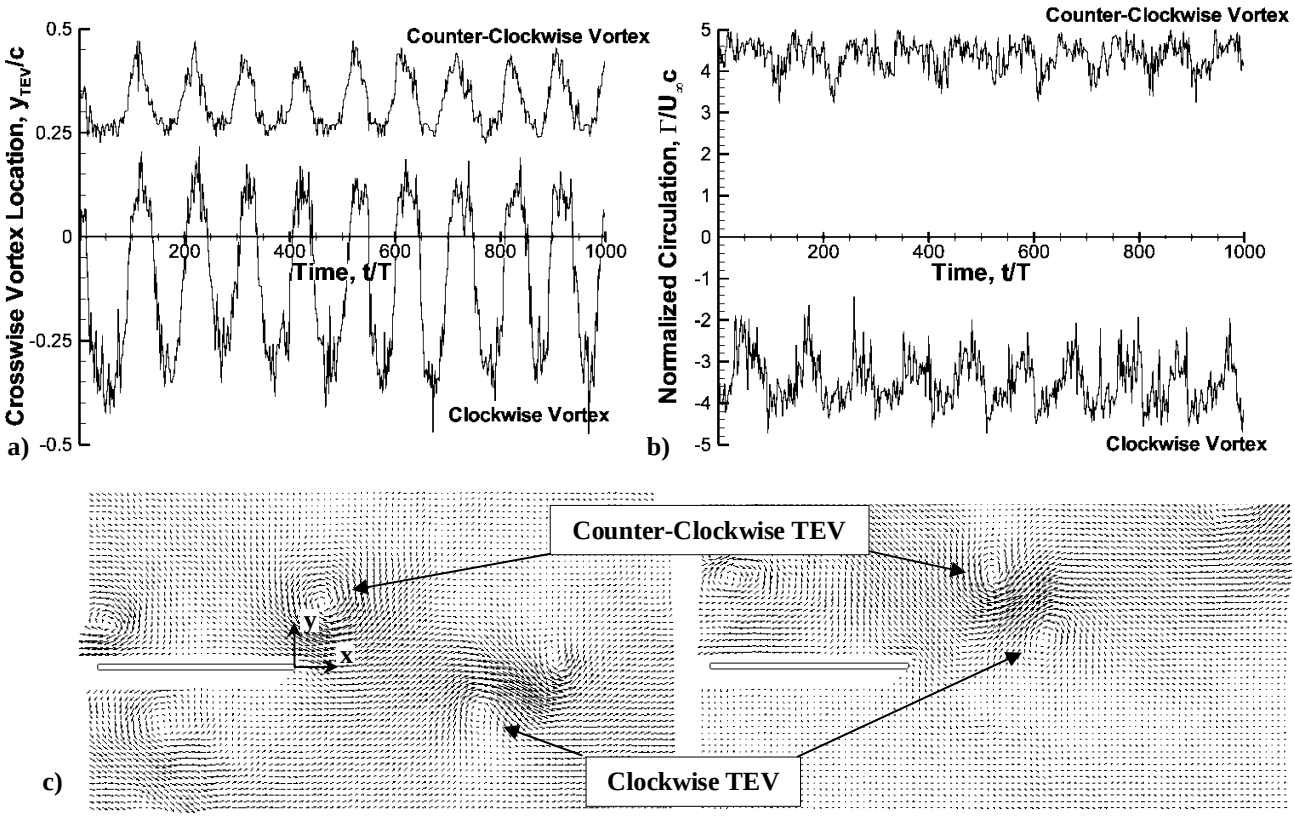

Fig. 10 a) Instantaneous cross-stream position of trailing-edge vortex as measured in phase-locked measurements at $h = -a$, b) Instantaneous normalized circulation as measured in phase-locked measurements at $h = -a$, c) Inset identifying clockwise and counter-clockwise vortex for two extreme cases.

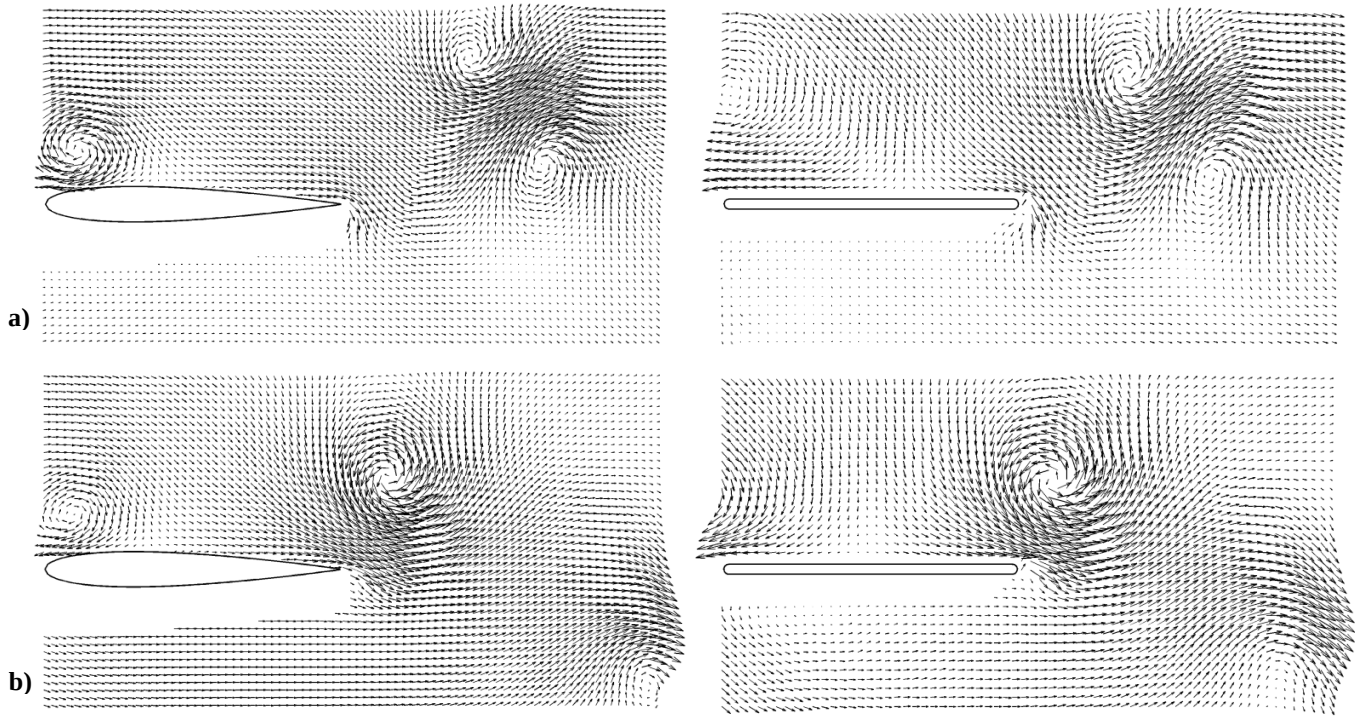

Fig. 11 Comparison of phase-averaged NACA 0012 bifurcation flow fields with their flat plate equivalents: a) mode A, and b) mode B.

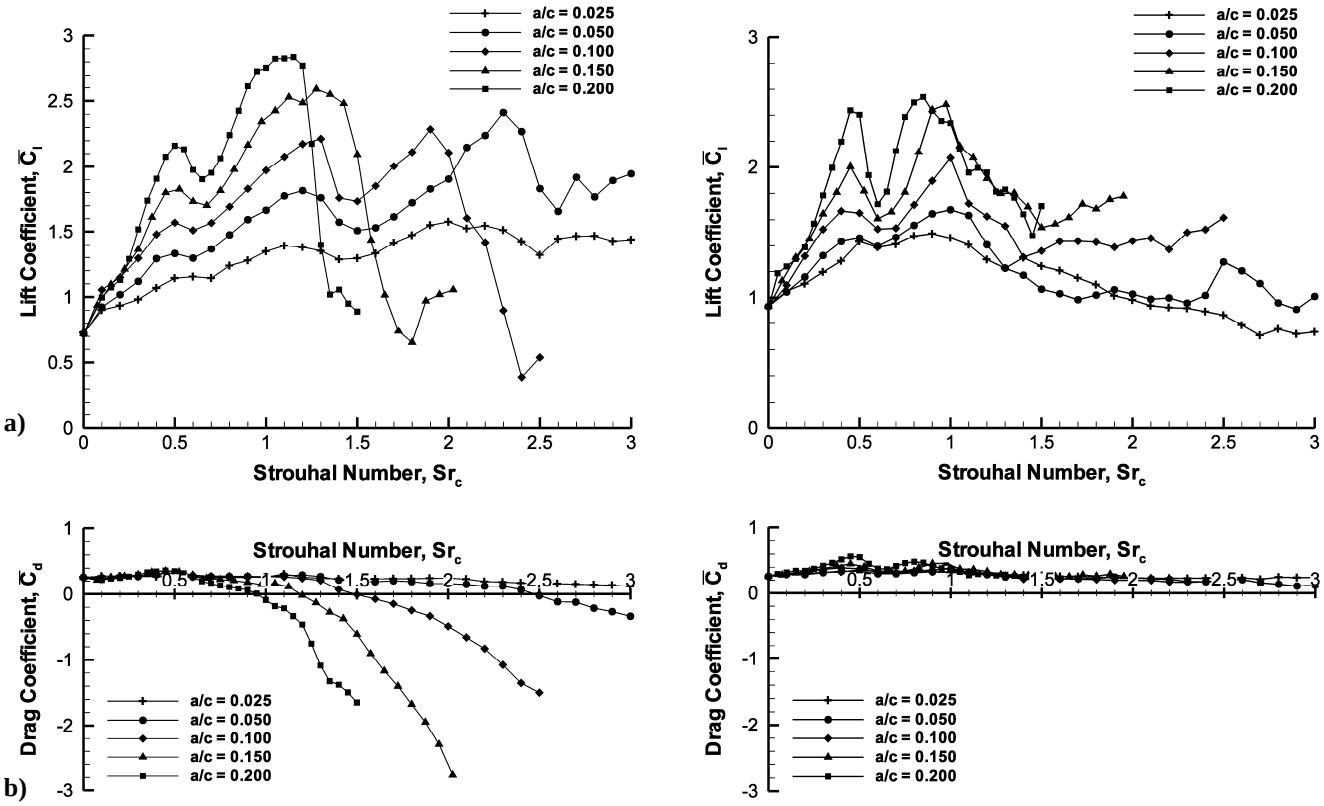

Fig. 12 a) Time-averaged lift coefficient, and b) drag coefficient plotted against Strouhal number based on chord for the NACA 0012 airfoil (left column) and the flat plate (right column) at α = 15°.

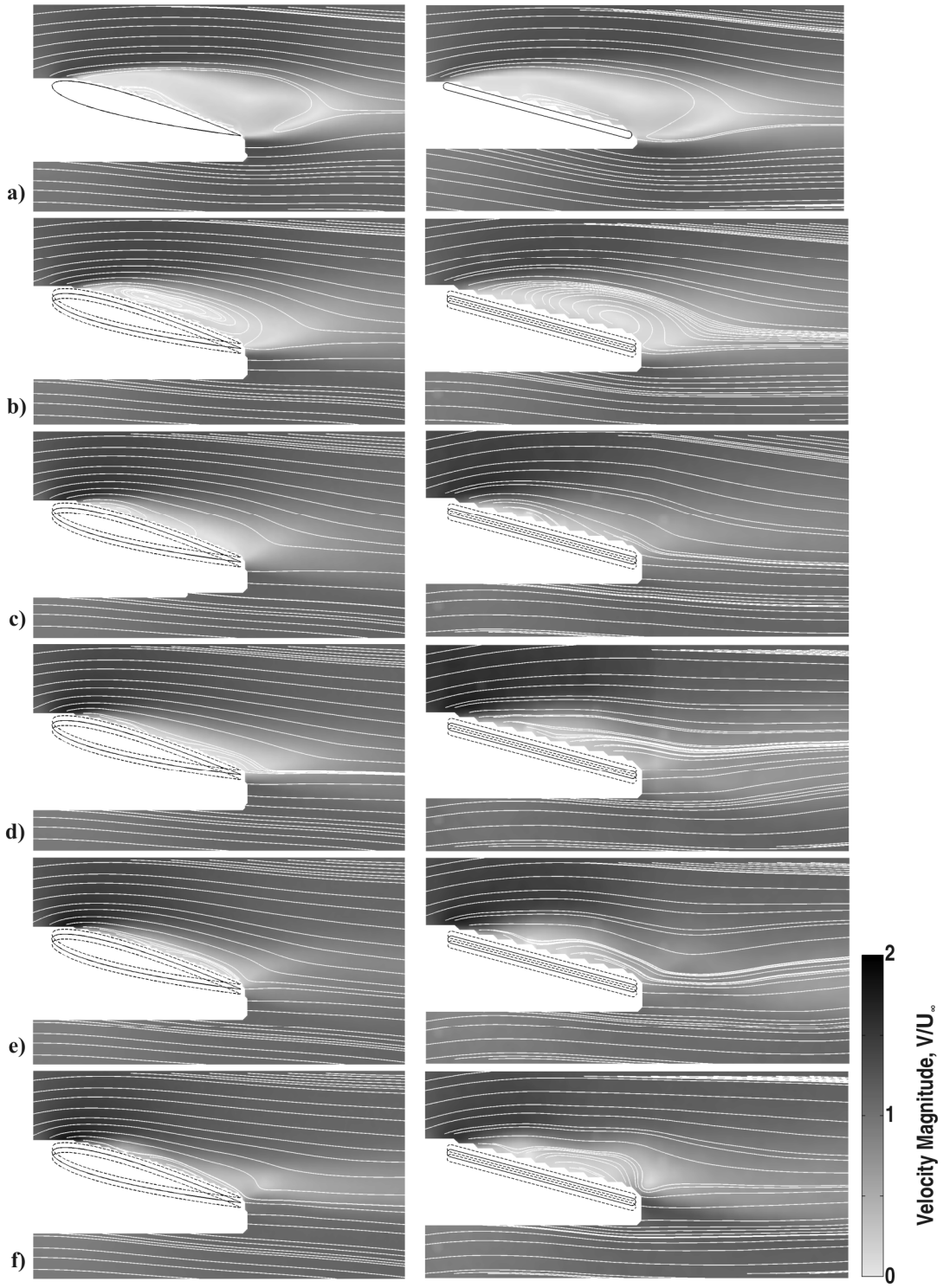

Fig. 13 Time-averaged velocity magnitude for the NACA 0012 airfoil (left column) and flat plate (right column) for a/c = 0.025 and α = 15° at Strouhal numbers of: a) Sr_c = 0, b) Sr_c = 0.25, c) Sr_c = 0.50, d) Sr_c = 0.75, e) Sr_c = 1.00, f) Sr_c = 1.25, g) Sr_c = 1.50, h) Sr_c = 1.75, i) Sr_c = 2.00, j) Sr_c = 2.25, k) Sr_c = 2.50, l) Sr_c = 2.75, and m) Sr_c = 3.00 . Continued on next page.

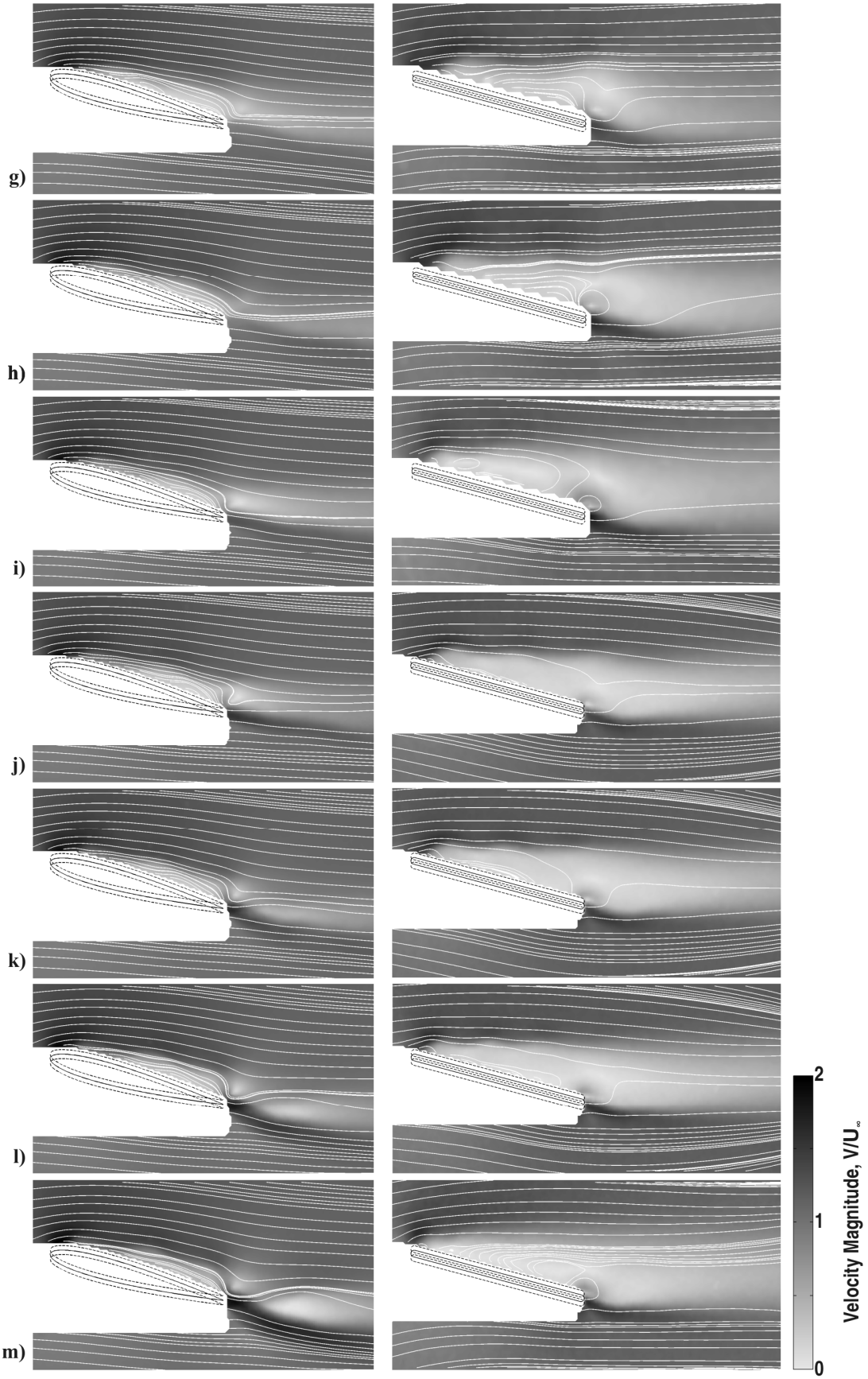

Fig. 13 Continued

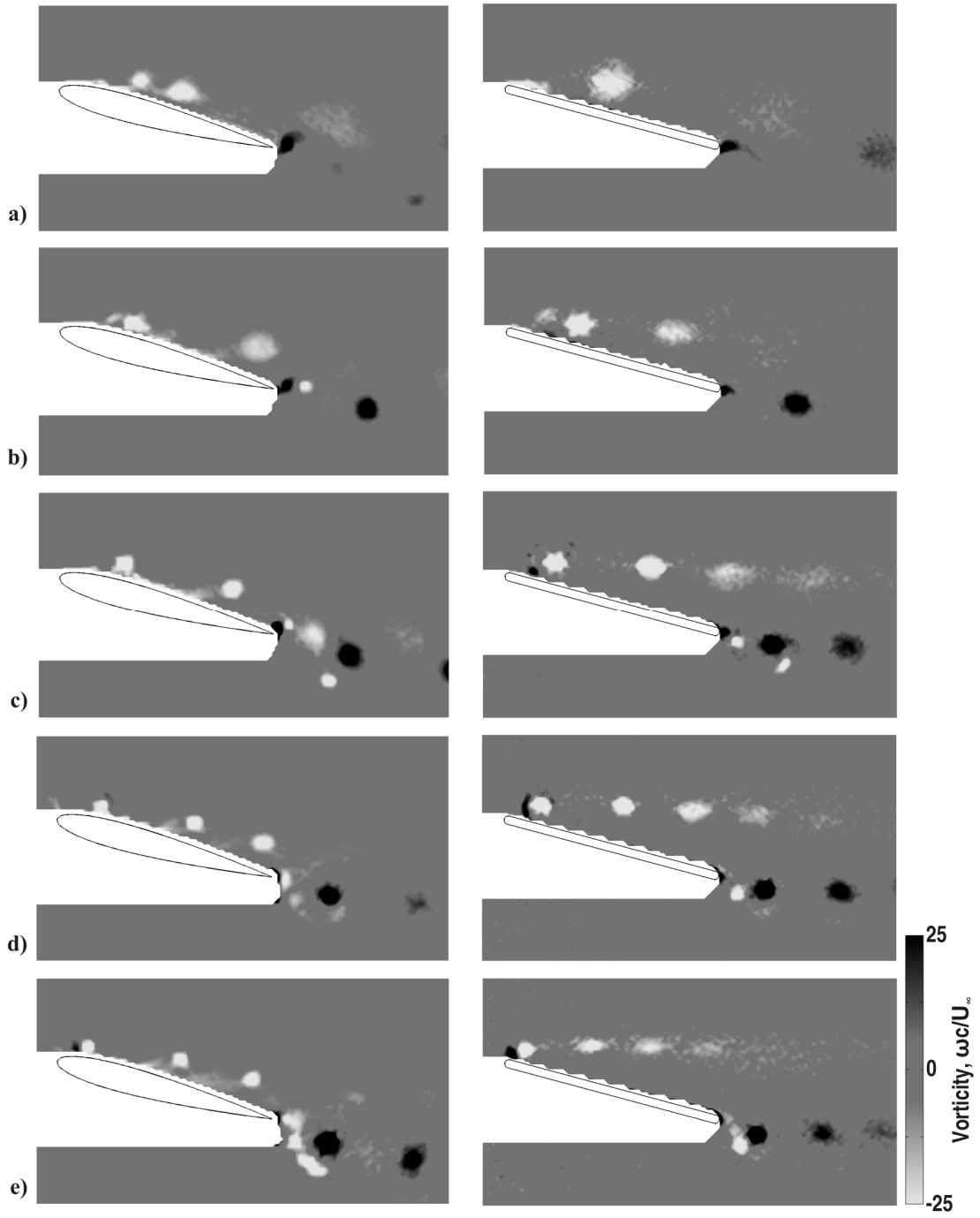

Fig. 14 Phase-averaged vorticity contour plots at the top of the motion for the NACA 0012 airfoil (left column) and flat plate (right column) for a/c = 0.025 and α = 15° at Strouhal numbers of: a) Sr_c = 1.00, b) Sr_c = 1.50, c) Sr_c = 2.00, d) Sr_c = 2.50, and e) Sr_c = 3.00.

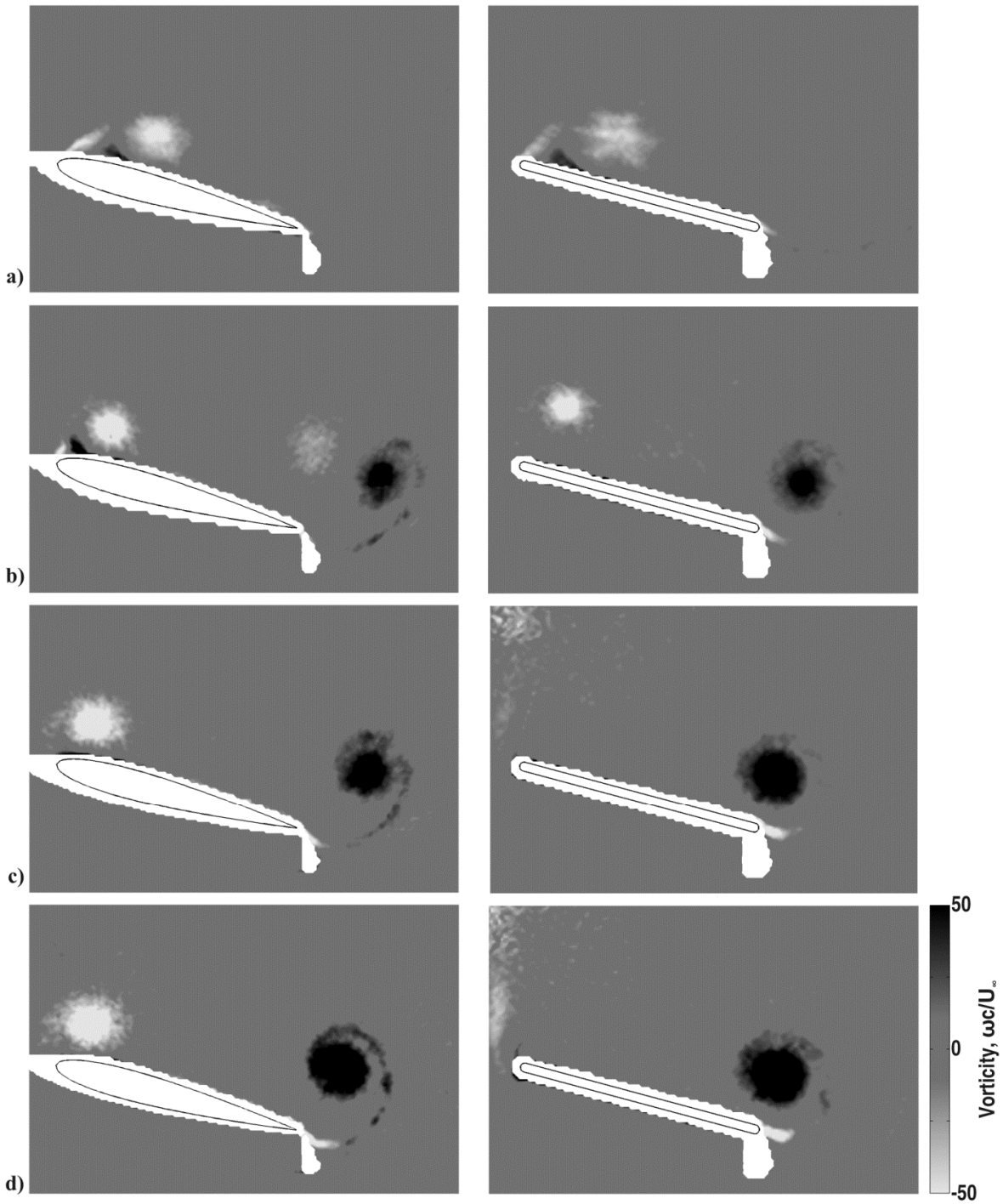

Fig. 15 Phase-averaged vorticity contour plots at the bottom of the motion for the NACA 0012 airfoil (left column) and flat plate (right column) for a/c = 0.150 and α = 15° at Strouhal numbers of: a) Sr_c = 0.50, b) Sr_c = 1.00, c) Sr_c = 1.50, and d) Sr_c = 2.00.

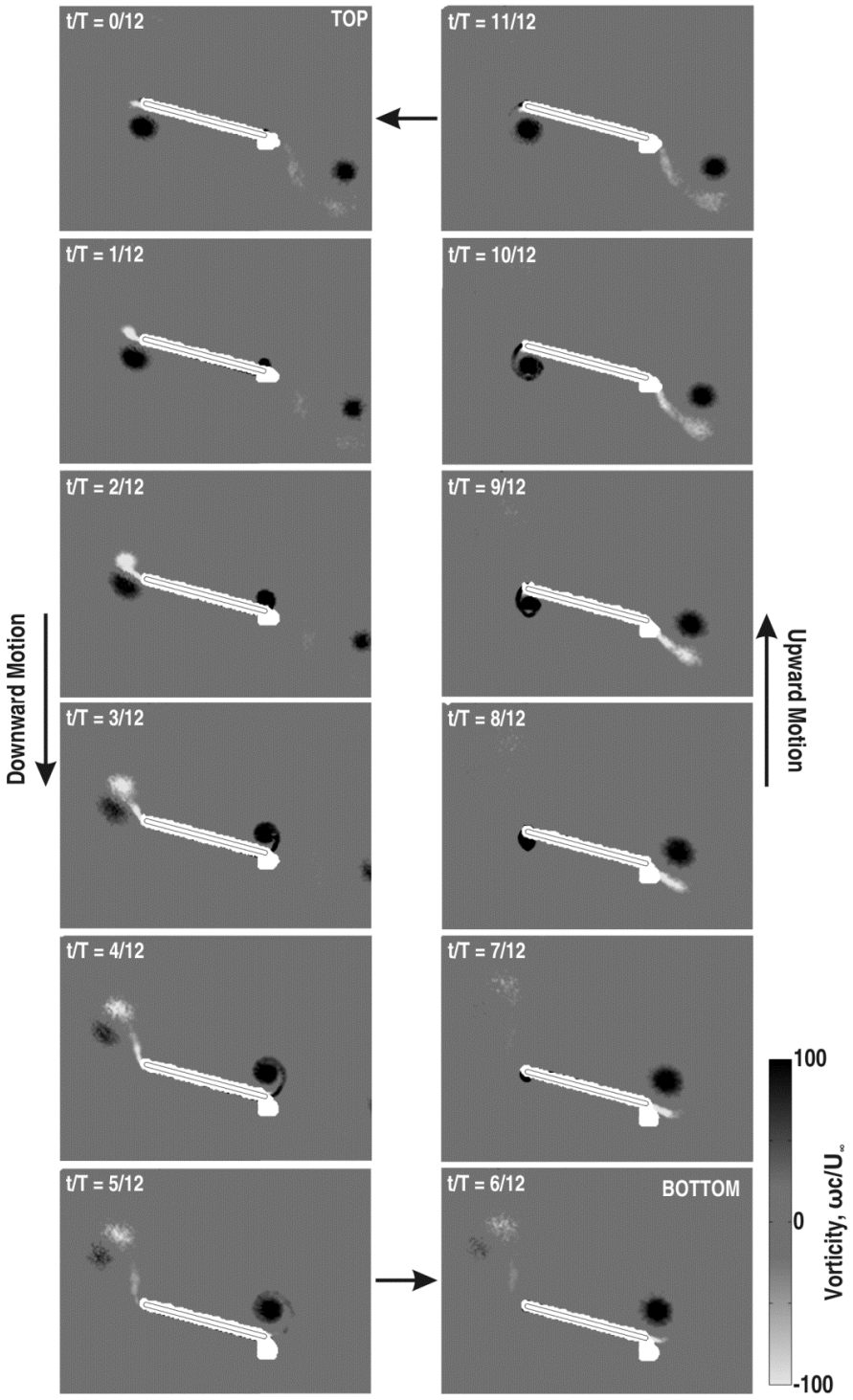

Fig. 16 Phase-averaged vorticity contour plots for the flat plate at twelve phases in the cycle for α = 15°, a/c = 0.15 and Sr_c = 2.00.

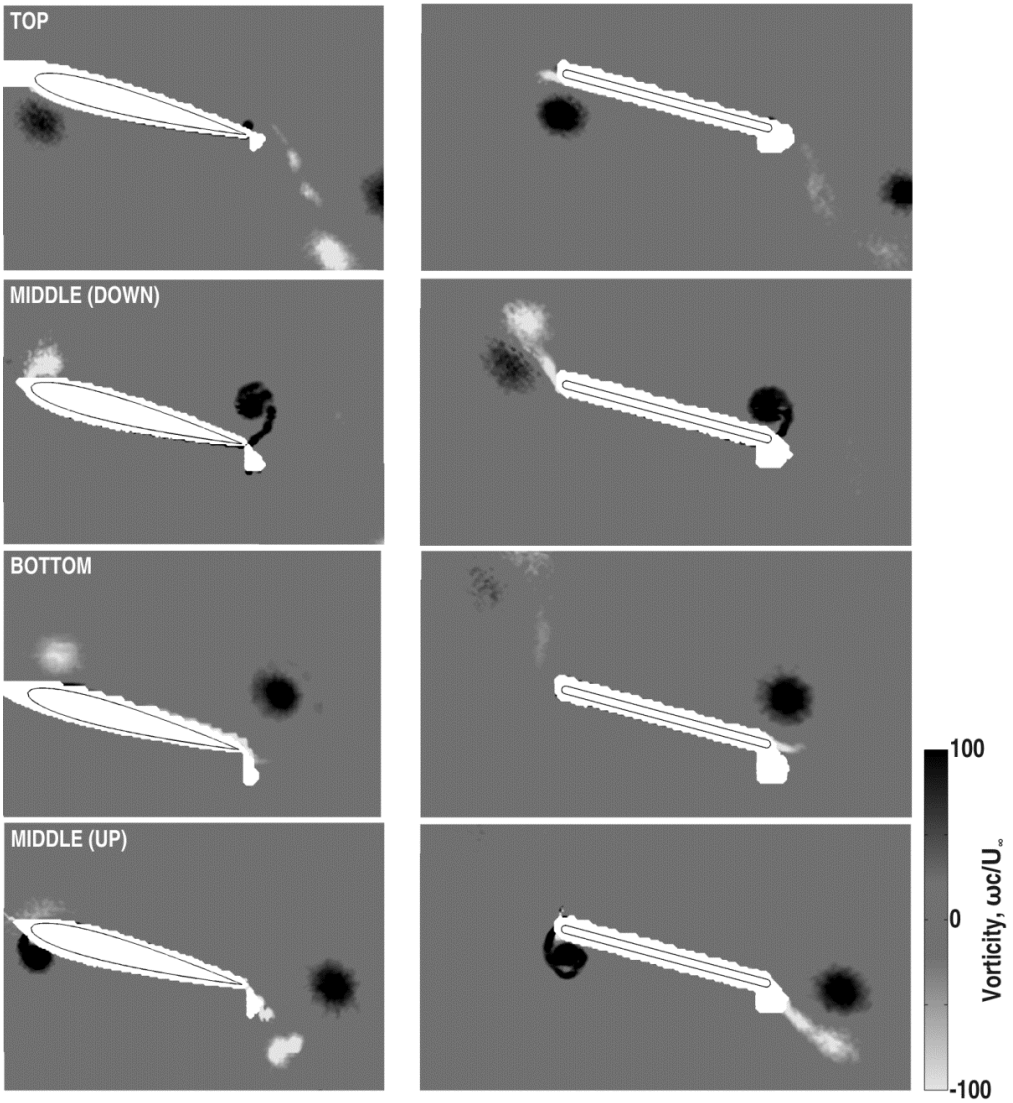

Fig. 17 Phase-averaged vorticity contour plots for the NACA 0012 airfoil (left) and flat plate (right) at four phases in the cycle for α = 15°, a/c = 0.15 and Sr_c = 2.00.

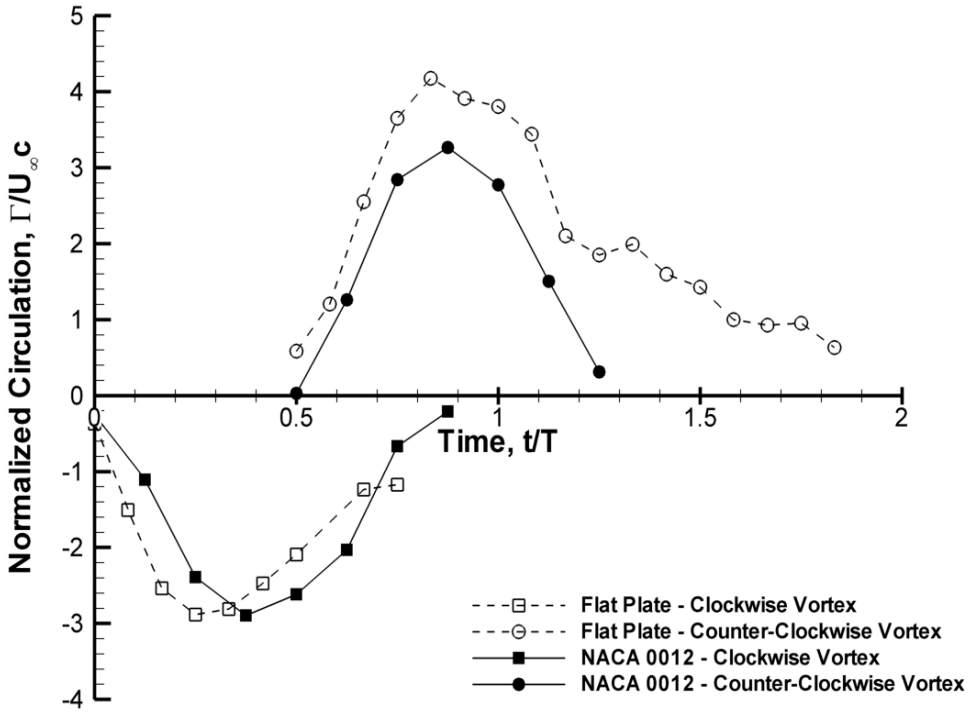

Fig. 18 Leading-edge vortex circulation from phase-averaged measurements for the NACA 0012 and flat plate airfoil for α = 15°, a/c = 0.15 and Sr_c = 2.00. Note the delayed formation of the clockwise vortex and premature formation of the counter-clockwise vortex for the flat plate.